Journal of
Materials Chemistry C

ROYAL SOCIETY
OF CHEMISTRY

PAPER

View Article Online
View Journal

Check for updates

Cite this: DOI: 10.1039/d0tc02941f

Deep-blue fluorescent emitter based on a 9,9-dioctylfluorene bridge with a hybridized local and charge-transfer excited state for organic light-emitting devices with EQE exceeding 8%†

Xing Liu,‡[a] Wen Liu,‡[a] Wu Dongyu,[b] Xiaozhen Wei,[a] Long Wang,[a] Hua Wang, *[a] Yanqin Miao, *[a] Huixia Xu, [a] Junsheng Yu [c] and Bingshe Xu*[a]

Received 21st June 2020,
Accepted 19th August 2020

DOI: 10.1039/d0tc02941f

rsc.li/materials-c

It is indispensable to synthesize deep-blue light emitting materials with high luminous efficiency for realizing full-colour organic light emitting diode (OLED) displays. The hybridized local and charge-transfer (HLCT) state is a special excited state that hybridizes the local state and the charge transfer state to ensure a high fluorescence quantum yield (η_{pl}). Herein, a blue fluorescent material of **TPA-DFCP** was designed and synthesized, with a twisted D–π–A configuration, in which triphenylamine (TPA), benzonitrile (CP) and 9,9-dioctylfluorene serve as the D, A, and π-conjugation unit, respectively. It also exhibits good solubility and can be dissolved in several organic solvents with different polarities. The non-doped device, with **TPA-DFCP** as the emitter, shows excellent electroluminescent (EL) efficiency with a maximum EQE of 7.74%. Furthermore, the doped device of **TPA-DFCP** exhibits excellent deep-blue emission with the EL emission peak at 436 nm and the CIE coordinates at (0.153, 0.077), which are very close to the NTSC standard blue CIE (x, y) coordinates of (0.140, 0.080). Meanwhile, the doped device also exhibited excellent EL performance, with a maximum external quantum efficiency (EQE) and radiative exciton utilization (η_r) of 8.30% and 57.67%, respectively.

Introduction

In recent years, organic light emitting diodes (OLEDs) have attracted wide attention arising from the advantages of low cost of fabrication, diversity of variety and structure, adjustable performance by structural design, and the simple synthesis process.[1–10] In order to realize full-colour OLED displays, it is indispensable to synthesize new light-emitting materials of three primary colours with high luminous efficiency, especially blue-light materials.[11–13] Luminescent materials usually form 25% singlet excitons and 75% triplet excitons. However, in traditional fluorescent materials, the 75% triplet excitons are prone to dissipate by thermal radiation. Hence, the use of the 75% triplet excitons is the key to improving the exciton utilization rate of the material. As yet, there are three major organic electroluminescence mechanisms using triplet excitons, *i.e.* triplet–triplet annihilation (TTA), thermally activated delayed fluorescence (TADF), and hybridized local and charge-transfer (HLCT).[14,15]

In TTA type luminescent materials, when there is a large energy level difference between the lowest singlet excited state (S_1) and the lowest triplet excited state (T_1), the TTA process occurs between the two triplet excitons, and the upper conversion produces a high-level triplet exciton (T_m) with similar energy levels to the high-level singlet (S_n), and then singlet excitons are generated by intersystem crossing (ISC) between T_m and S_n, leading to high-efficiency fluorescence emission.[16–18] However, the theoretical upper limit of the singlet exciton production ratio is still less than 62.5% when the TTA process occurs, corresponding to an external quantum efficiency (EQE) of 12.5% in the ideal case.[16,19] For TADF materials, it is important to realize the efficient reverse intersystem crossing (RISC) process of excitons from T_1 to S_1.[20–23] In order to promote the RISC process, the energy level difference (ΔE_{ST}) between T_1 and S_1 must be small enough through the complete separation of the HOMO and LUMO of the material to enhance the CT state. But, at the same time, TADF materials are prone to generate quenching of triplet

---

[a] *Key Laboratory of Interface Science and Engineering in Advanced Materials, Ministry of Education, Taiyuan University of Technology, Taiyuan 030024, China. E-mail: wanghua001@tyut.edu.cn, miaoyanqin@tyut.edu.cn, xubs@tyut.edu.cn*
[b] *SEDIN Engineering Co., Ltd, Taiyuan 030000, China*
[c] *State Key Laboratory of Electronic Thin Films and Integrated Devices, School of Optoelectronic Information, University of Electronic Science and Technology of China, Chengdu 610054, China*

† Electronic supplementary information (ESI) available. CCDC 2010880. For ESI and crystallographic data in CIF or other electronic format see DOI: 10.1039/d0tc02941f

‡ These authors contributed equally to this work.

excitons, leading to roll-off of the efficiency and a short lifetime of devices in the process of electroluminescence.[24,25] The HLCT state is a special excited state that hybridizes the local state and the charge transfer state.[26] The LE state ensures that the material has a high fluorescence quantum yield (η_{pl}), and the CT state guarantees that the material has a high exciton utilization rate.[11,27,28] Theoretically, the exciton utilization rate of HLCT materials can reach 100%. Moreover, the luminescence of the HLCT material originates from the LE state, so the emission spectrum is narrower, and the colour purity of the device is higher. The coexistence of the CT state and the LE state of HLCT materials requires that the HOMO and LUMO of the material overlap and separate, and the rigidity of the structure is small. In 2015, Tang *et al.* constructed a donor–acceptor (D–A) type molecule named PMSO with phenanthroimidazole as a weak donor and sulfone as a moderate acceptor, and achieved a maximum EQE of 6.85% with an emission peak of 445 nm and CIE coordinates (0.152, 0.077) for the doped device.[28] In 2019, Qiu *et al.* reported HLCT state materials of 9,9-dimethyl-*N*,*N*-diphenyl-7-(1,4,5-triphenyl-1*H*-imidazol-2-yl)-9*H*-fluoren-2-amine (DFPBI) and 4-(9,9-dimethyl-7-(1,4,5-triphenyl-1*H*-imidazol-2-yl)-9*H*-fluoren-2-yl)-*N*,*N*-diphenylaniline (TFPBI) with a structure of donor–π–acceptor (D–π–A) with 9,9-dimethylfluorene as the π-bridge, and achieved a maximum EQE of the doped device of TFPBI of 6.01%, with CIE coordinates (0.153, 0.051).[29] In summary, HLCT materials have great potential for the design of deep-blue emitters.

In this work, blue fluorescent material **TPA-DFCP** was designed and synthesized, with a twisted D–π–A configuration, in which triphenylamine (TPA), benzonitrile (CP) and 9,9-dioctylfluorene serve as the D, A, and π-conjugation unit, respectively. Herein, TPA is a strong electron donor group and has a high HOMO energy level. More importantly, the molecular space of TPA has a certain twist angle for avoiding the accumulation of molecules to construct the intramolecular CT state.[30] 9,9-dioctylfluorene, known as a common rigid π-conjugated bridge, provides necessary conjugation to the molecular backbone, and thus ensures the satisfactory contribution of the LE component for the HLCT state and improves η_{pl} of fluorescent molecules.[31–33] Fortunately, the HLCT state was observed from the material **TPA-DFCP**. Meanwhile, the doped device of **TPA-DFCP** exhibits excellent deep-blue emission with the EL emission peak at 436 nm and the CIE coordinates at (0.153, 0.077), which are very close to the NTSC standard blue CIE (x, y) coordinates of (0.140, 0.080). Furthermore, the doped device also exhibited excellent EL efficiency, with a maximum EQE of 8.30%.

Results and discussion

Structure characteristics

The synthetic routes of **TPA-DFCP** can be seen in Scheme 1. The intermediate compound **M1** and the target products were prepared through a palladium catalysed Suzuki coupling reaction, and then purified by column chromatography on silica gel.

Single crystals of **TPA-DFCP** were obtained through slow diffusion of ethanol into methylene dichloride, and then a suitable crystal was selected. The crystal system of **TPA-DFCP** is monoclinic, the space group is *I*2/*a* and there were eight molecules in one unit cell. As shown in Fig. 1a, the twisted dihedral angle between the TPA substituents and the central 9,9-dimethylfluorene was 37.49° (θ_1), and the dihedral angle between benzonitrile and the central 9,9-dimethylfluorene was 38.89° (θ_2), which is similar to the dihedral angle from theoretical calculations. As presented in Fig. 1b, the N-atom of benzonitrile and the benzonitrile-H of the adjacent molecules form C–H···N hydrogen bonds.

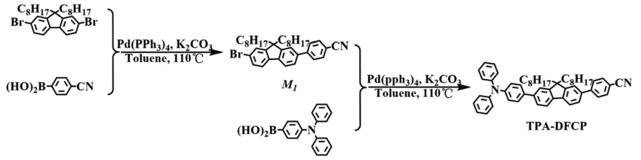

Scheme 1 Synthetic route of **TPA-DFCP**.

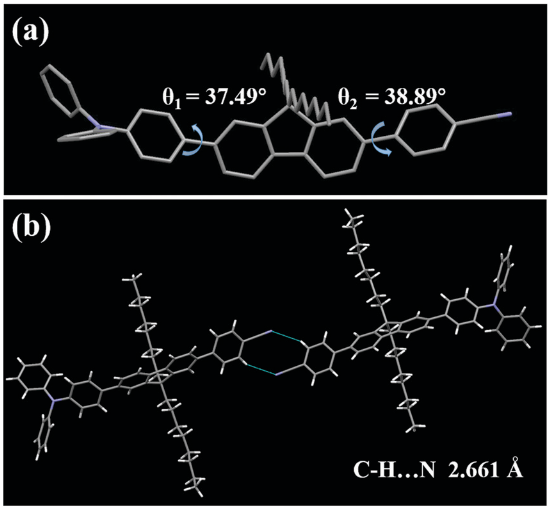

Fig. 1 (a) A single molecular structure of the **TPA-DFCP** crystal; (b) intermolecular interactions.

To further explore the relationship between the material property and molecular structure of **TPA-DFCP**, the electronic structure was calculated, and the optimized structures and frontier molecular orbital distributions are shown in Fig. 2. As depicted, the HOMO and LUMO of **TPA-DFCP** are mainly distributed on the D unit of TPA and the A unit of CP, respectively. The separation of the electron density distribution of the HOMO and LUMO indicates the existence of a CT state. Meanwhile, a certain degree of overlap between the HOMO and LUMO of **TPA-DFCP** distributed on the π-conjugation unit of DF

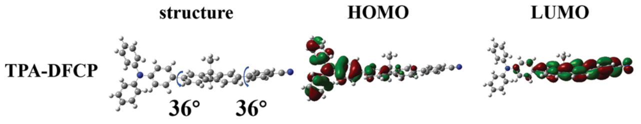

Fig. 2 Optimized structures and frontier molecular orbital distributions of **TPA-DFCP**.

indicates a decent radiative transition rate for this material to achieve high η_{pl}.

Photophysical properties

In order to investigate the photophysical properties, UV-vis absorption and PL spectra of **TPA-DFCP** in different polar solutions and in a film were measured (Fig. 3, Fig. S3, ESI,† and Table 1). As shown in Fig. 3a, the UV-vis absorption spectrum of **TPA-DFCP** in dilute toluene solution exhibits an absorption peak at 300 nm, and a maximum absorption peak at 368 nm, corresponding to the n–π* transition between n electrons and π electrons on N heteroatoms of triphenylamine, and the π–π* transition of the whole molecule, respectively. The PL spectrum in dilute toluene solution exhibits a maximum emission peak (λ_{pl}) at 433 nm. In the film, the UV-vis absorption spectrum of **TPA-DFCP** exhibits similar features as in dilute solutions: the PL spectrum of **TPA-DFCP** in the film shows a 21 nm red-shift relative to that in toluene solution, which is owing to molecule aggregation (Fig. 3a).

In addition, for researching the CT characteristic in excited states, the photophysical properties of **TPA-DFCP** in different solvents were examined (Fig. S3, ESI†). As shown, from low-polarity (*i.e.* hexane, f = 0.0012) to high-polarity solutions (*i.e.* acetonitrile, f = 0.305), the emission peaks in the PL spectra of **TPA-DFCP** show a large redshift of 126 nm. The significant solvation effect originates from CT from the D unit of TPA to the A unit of CP, which indicates that the **TPA-DFCP** molecule is more likely to be affected by the solvent polarity during the radiative transition, and the excited states have strong CT characteristics. Subsequently, the relationship between the Stokes shift ($\nu_a - \nu_f$) and the orientation polarizability of the solvent $f(\varepsilon, n)$ was investigated to estimate the dipole moment of the S_1 state (μ_e), according to the Lippert–Mataga equation as introduced in previously reported work.

$$hc(\nu_a - \nu_f) = hc(\nu_a{}^0 - \nu_f{}^0) + \frac{2(\mu_e - \mu_g)^2}{\alpha_0{}^3} f(\varepsilon, n)$$

As presented in Fig. 3b, **TPA-DFCP** shows two linear relationships between the Stokes shift and the orientation polarizability of solvents. According to the calculation, μ_e of **TPA-DFCP** in low polarity solvents (6.36 D) is smaller than the well-known CT molecule 4-(*N*,*N*-dimethylamino)benzonitrile (DMABN) (23 D), and μ_e of TPA(PFCP) in high polarity solvents (31.76 D) is larger than 23 D, which indicates that the excited state of **TPA-DFCP** exhibits a mixed character of LE and CT states: the LE-dominated excited state in low polarity solvents ($f < 0.096$), the CT-dominated excited state in high-polarity solvents ($f > 0.149$), and an inter-crossed excited state of LE character and CT character in environments with moderate polarity ($0.096 < f < 0.149$). Moreover, η_{pl} of **TPA-DFCP** in different polar solvents was measured (82.76% in hexane; 79.96% in chloroform; 53.17% in acetonitrile), and η_{pl} showed a significant decreasing trend with increasing solvent polarity, which coincided with the increase of the CT states above.

In order to further investigate the excited state properties, transient PL decay of **TPA-DFCP** in different solutions and in a film was measured. As shown in Fig. S4 and Table S2 (ESI†), the spectra illustrate that **TPA-DFCP** shows short PL decay lifetimes

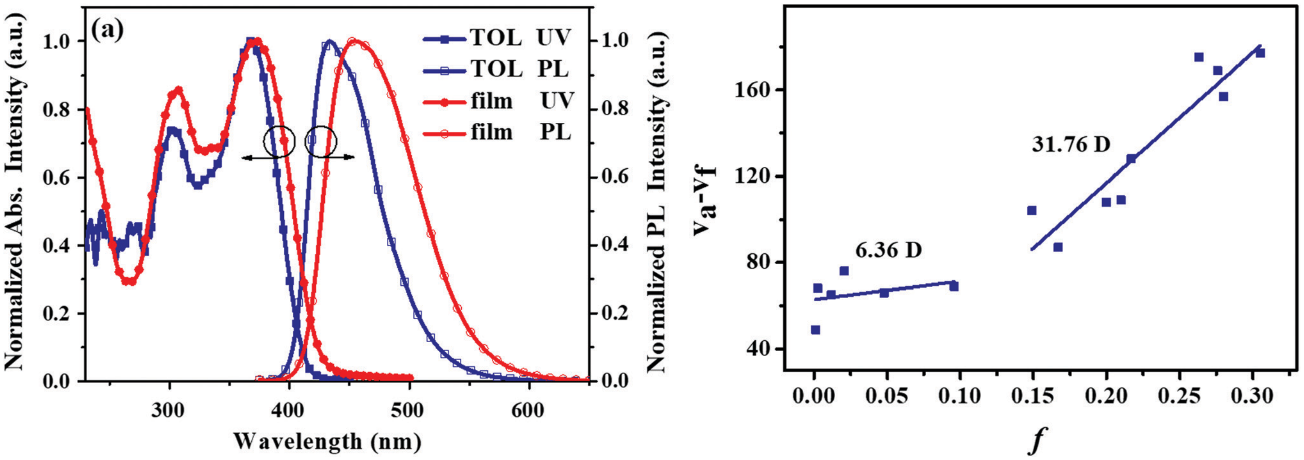

Fig. 3 (a) UV-vis absorption and PL spectra of **TPA-DFCP** in toluene solution and in a film; (b) fitted correlation of the Stokes shift as a function of solvent polarity.

Table 1 The photophysical, electrochemical and thermal properties of **TPA-DFCP**

	λ_{pl} [nm]		λ_{abs} [nm]						
Compound	Solution	Film	Solution	Film	η_{pl} [%]	HOMO/LUMO [eV]	T_d [°C]	T_g [°C]	$\Delta E_{ST}{}^b$ [eV]
TPA-DFCP	433	454	368	368	66.74	−5.29/−2.31	398	—[a]	0.37

Measured in [a] Not observed. [b] $\Delta E_{ST} = E(T_1) - E(S_1)$

ranging from 1.20 to 3.22 ns in different solvents and a film. Based on the fluorescence lifetime of **TPA-DFCP** film (τ = 2.26 ns), the radiative decay rate ($k_r = \eta_{pl}/\tau_f$) and non-radiative decay rate ($k_{nr} = 1/\tau_f - k_r$) can be calculated to be 0.295 and 0.147 ns^{-1}, respectively. Obviously, the value of k_r is much larger than that of k_{nr}, which originates from the intramolecular planarization. As illustrated in Fig. S5 (ESI†), the emission peaks of the PL spectra at room temperature and phosphorescence spectra at 77 K were located at 467 and 543 nm, respectively. According to the formula $\Delta E_{ST} = 1240/\lambda_{Fl} - 1240/\lambda_{Ph}$, ΔE_{ST} between the S_1 and T_1 states is as high as 0.372 eV, indicating that the RISC transition from the T_1 to the S_1 state is impossible during the PL process. In consideration of the large ΔE_{ST} and short PL decay lifetime, we have excluded the TADF mechanism for the **TPA-DFCP** luminescence process.

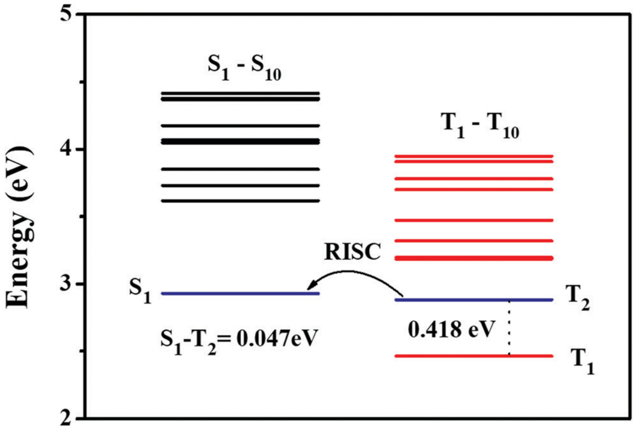

Fig. 4 The energy landscape of singlet and triplet excited states for the BTDF-based compounds of **TPA-DFCP**.

Moreover, the energy landscape of singlet and triplet excited states was calculated to observe the excited state performance of **TPA-DFCP** (Fig. 4). It can be known from Fig. 4 that the large energy gap between T_2 and T_1 ($\Delta E_{T_2-T_1}$ = 0.42 eV) may significantly prohibit internal conversion from T_2 to T_1 on the basis of the energy gap law, and the small energy gap between T_2 and S_1 ($\Delta E_{T_1-S_1}$ = 0.05 eV) may be facilitating reverse intersystem crossing (RISC) from T_2 to S_1. Such an energy level landscape meets the requirement of the ''hot exciton'' mechanism very well, leading to a high-lying RISC process from T_2 to S_1, and an exciton utilization exceeding 25% under electrical excitation can be expected.

Electroluminescence performance

To investigate the electroluminescence (EL) performance of **TPA-DFCP**, we fabricated a blue OLED with a non-doped configuration (Fig. 5): ITO/MoO_3 (3 nm)/TAPC (40 nm)/TCTA (10 nm)/**TPA-DFCP** (20 nm)/TmPyPB (30 nm or 40 nm)/LiF (1 nm)/Al (120 nm) (named Device A or B), in which MoO_3 was employed as the hole-injection layer (HIL), 4,4′-cyclohexylidene bis[*N*,*N*-bis(*p*-tolyl)aniline] (TAPC) served as the

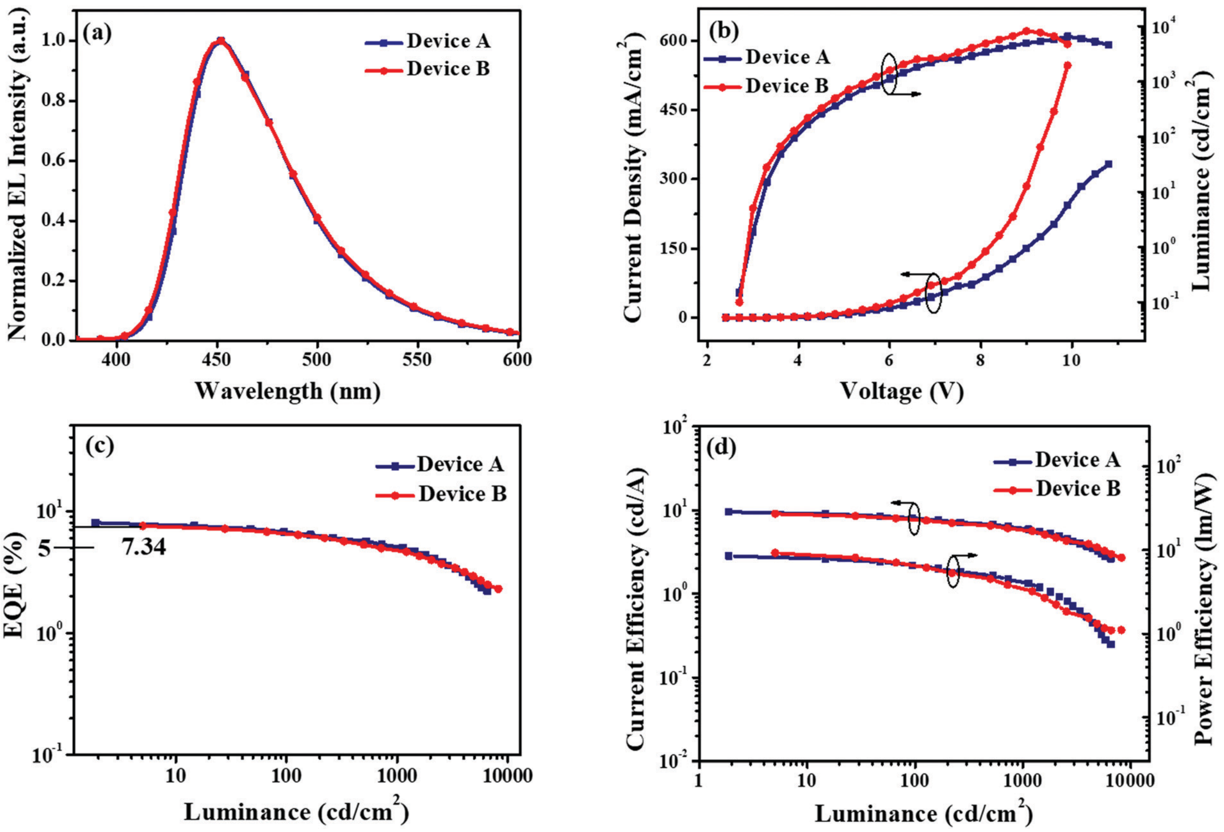

Fig. 5 EL performance of Device A and Device B: (a) EL spectra, the picture of Device B; (b) *J*–*V*–*L* curve; (c) CE–*L*–PE curve; (d) EQE–*L* curve.

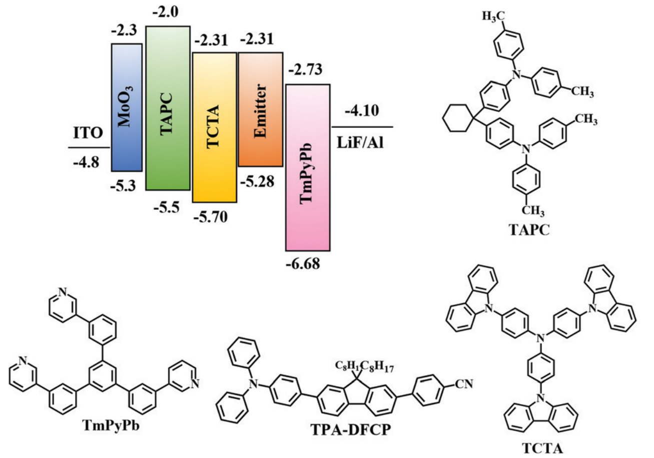

Scheme 2 Schematic energy level diagram of the devices based on **TPA-DFCP**.

hole-transporting layer (HTL), 4,4′4″-tri(*N*-carbazolyl)-triphenyl amine (TCTA) acted as a buffer for confining excitons within the emission layer, 1,3,5-tri(*m*-pyrid-3-ylphenyl)benzene (TmPyPb) acted as the electron-transporting layer (ETL), and LiF acted as the electron-injection layer (Scheme 2). For Device A and Device B, the ETL has different thicknesses. As shown in Fig. 5, the two devices had a deep-blue emission peak at 452 nm, consistent with the PL emission of the thin film, indicating that the emission was from only **TPA-DFCP** rather than other layers or any exciplex formed. Meanwhile, the two devices exhibited excellent color stability since the EL spectra showed nearly no changes with increasing driving voltage (Fig. S6, ESI†); the similar CIE coordinates of the devices are located at (0.155, 0.140) (Device A) and (0.156, 0.141) (Device B). As shown in Fig. 5, Device A exhibits higher EL efficiency with a maximum EQE of 7.74%, a turn-on voltage (V_{on}) of 2.90 V, a maximum current efficiency (CE) of 9.21 cd A^{-1} and a maximum power efficiency (PE) of 9.17 lm W^{-1} relative to those of Device B (EQE = 7.34%, V_{on} = 2.9 V, CE = 8.76 cd A^{-1}, and PE = 9.17 lm W^{-1}). Meanwhile, however, Device B has better maximum brightness with 8212 cd m^{-2} compared with Device A (L_{max} = 6540 cd m^{-2}). Meanwhile, η_s of Device A and Device B was estimated to be 57.99% and 54.99%, which are higher than the upper limit of η_s (25%) for traditional fluorescent materials. Higher η_s indicates that the molecule can effectively utilize some of the triplet excitons to participate in the luminescence, and thus a higher EQE was obtained, which is in line with our original intention to design molecules.

To further improve the EL efficiency and colour purity of Device B, different doped devices were fabricated with 4,4′-bis-(*N*-carbazolyl)-1,1′-biphenyl (CBP) as the host, and **TPA-DFCP** as the dopant. Through changing the doping ratio, different doped devices were obtained: ITO/MoO_3 (3 nm)/TAPC (40 nm)/TCTA (10 nm)/CBP : 5 wt%, 10 wt%, 15 wt%, 30 wt%, 50 wt%, 80 wt% **TPA-DFCP** (20 nm)/TmPyPB (40 nm)/LiF (1 nm)/Al (120 nm), where the doping concentrations of 5 wt%, 10 wt%, 15 wt%, 30 wt%, 50 wt% and 80 wt% correspond to Devices B1, B2, B3, B4, B5, and B6, respectively (Fig. S8 (ESI†) and Fig. 6). As shown in Table S3 (ESI†), compared to the non-doped device B, the doped devices B1–B6 exhibit obvious blue-shifted EL spectra, and with the decrease of the doping concentration, the blue-shift value for the EL spectra presents an increasing trend. This is because the interactions between **TPA-DFCP** molecules in the doped devices are obviously weaker than in the non-doped device B, which leads to a relatively large band gap in the doped devices, further inducing blue-shifted EL spectra. The blue-shift of the EL spectra also causes the reduced luminance and current efficiency for the corresponding devices. It's easy to understand because the luminance depends on the human vision function, where emission with a peak of 555 nm for the same photonic radiation shows the strongest emission luminance, and emission with a longer or shorter waveband will exhibit reduced luminance for the same photonic radiation. Especially, as shown in Fig. 6 and Table 2, Device B1 showed high quality deep blue light emission with the EL spectral emission peak at 436 nm and the CIE coordinates at (0.153, 0.077). Furthermore, Device B1 also exhibited excellent EL efficiency, with a maximum EQE, CE and PE of 8.30%, 5.63 cd A^{-1}

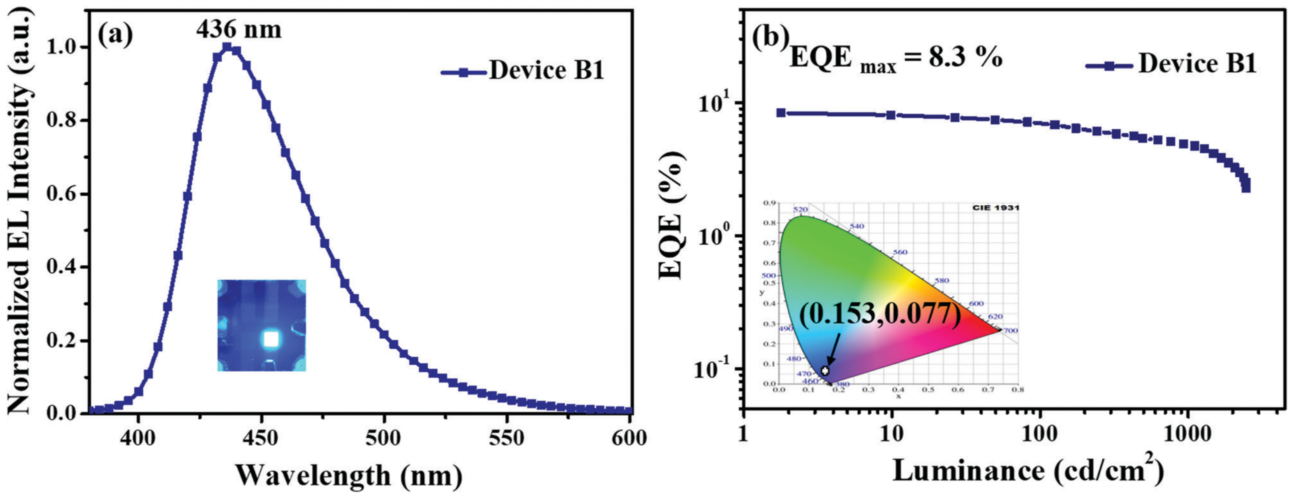

Fig. 6 EL performance of Device B1: (a) EL spectra, the picture of Device B1; (b) EQE–*L* curve and CIE coordinates.

Table 2 EL performance of devices based on **TPA-DFCP**

TPA-DFCP	λ_{EL} [nm]	CIE (x, y)	EQE$_{max}$ [%]	CE$_{max}$ [cd A^{-1}]	PE$_{max}$ [lm W^{-1}]	L_{max} [cd m^{-2}]	V_{on}[a] [V]
Device A	452	(0.155, 0.140)	7.74	9.21	9.25	6540	2.90
Device B	452	(0.155, 0.141)	7.34	8.76	9.17	8212	2.90
Device B1	436	(0.153, 0.077)	8.30	5.63	4.87	2482	3.54

[a] Turn-on voltage estimated at a brightness of 1 cd m^{-2}.

Table 3

Compound	λ_{EL} (nm)	CIE (x, y)	EQE$_{max}$ (%)	Ref.
TPA-DFCP	436	(0.153, 0.077)	8.30	This work
PMSO	445	(0.152, 0.077)	6.85	28
DFPBI	425	(0.157, 0.039)	4.96	29
TFPBI	440	(0.153, 0.051)	6.01	29
TPEA	445	(0.150, 0.090)	8.00	34
PIMNA	412	(0.160, 0.034)	2.43	35
PyINA	440	(0.157, 0.084)	3.68	36
2EHO-CNPE	452	(0.150, 0.090)	7.06	36
3a	443	(0.150, 0.080)	7.10	37
CzPAF–TFMP	436	(0.155, 0.066)	5.40	38
***m*-BBTPI**	428	(0.160, 0.060)	3.63	39
Ph–BPA–BPI	448	(0.150, 0.080)	4.56	40

and 4.87 lm W^{-1}, respectively Table 3 summarized performance of the reported deep-blue OLEDs. As far as we know, the **TPA-DFCP**-based doped device realized a relatively outstanding performance in deep blue light emission. The excellent EL performance of Device B1 can be attributed to the addition of CBP, which can reduce the fluorescence quenching phenomenon caused by molecular packing, and promote efficient Förster energy transfer from CBP to **TPA-DFCP**.

Conclusions

In general, a blue-emitting compound **TPA-DFCP** was successfully designed and synthesized, which was based on triphenylamine and benzonitrile as D and A moieties, and 9,9-dimethylfluorene as the π-conjugation bridge. By theoretical calculations and experimental results, it is concluded that this material could be suitable with HLCT state, which possesses highly hybridized LE and CT excited states. The solvatochromic effect showed that the emission peak is less influenced by the polarity of the solvent in a low-polarity solvent, and the excited state shows the LE state characteristic; the emission peak is influenced by the polarity of the solvent in a high-polarity solvent, and the characteristic of the CT state is exhibited. Furthermore, the **TPA-DFCP** doped device exhibited high-efficiency deep-blue OLED performance with the EL spectral emission peak at 436 nm and the CIE coordinates at (0.153, 0.077) and a maximum EQE of 8.3%.

Experimental section

Materials and methods

All commercially available reagents were not further purified, unless otherwise specified. The solvents were purified by conventional procedures. ^{1}H NMR and ^{13}C NMR spectra were measured on a Bruker DRX 600 spectrometer where tetramethylsilane was used as an internal reference for chloroform deuteride. The crystal was kept at 293.41(10) K during data collection. Using Olex2, the structure was solved with the SHELXS structure solution program using direct methods and refined with the SHELXL refinement package using least squares minimization. Ultraviolet-visible (UV-vis) absorption and photoluminescence (PL) spectra were recorded on a Hitachi U-3900 and Horiba Fluoromax-4 spectrophotometer, respectively. Furthermore, transient fluorescence and low temperature phosphorescence spectra were measured using an Edinburgh FLS 980 spectrometer with a 375 nm xenon laser source. The HOMOs of the materials were measured using an ionization energy measurement (IPS) system, and the LUMOs were calculated from the HOMO and the optical band gap of the material. Thermal gravimetric analysis (TGA) curves were recorded on a Netzsch TG 209 F3 at a heating rate of 10 °C min^{-1} from 40 to 800 °C under a nitrogen flow.

Theoretical calculations

The electronic structure was calculated by TD-DFT calculations using the Gaussian suite of programs (Gaussian 09-B01 package). The ground state geometry was optimized at the B3LYP/6-311G*(d,p) level. The energy landscape of singlet and triplet excited states was calculated at the level of TD-M062X/6-31G(d,p) on the BTDF-based compounds.

OLED fabrication and characterization

OLEDs with an area of 3 × 3 mm^{2} were fabricated by vacuum deposition onto indium tin oxide (ITO) glass substrates. Current density–voltage–luminance (*J*–*V*–*L*) curves were measured on a Keithley 2400 source meter and BM-7A spot brightness meter. The electroluminescence (EL) spectra were measured through a PR-655 Spectra Scan spectrometer with computer control. EQEs were calculated from the *J*–*V*–*L* curves and EL spectra data. All the measurements were performed at room temperature.

Synthesis

All the reagents and solvents used for the syntheses and measurements were purchased from commercial suppliers and were used without further purification unless otherwise noted.

Synthesis of 4-(7-Bromo-9,9-dioctyl-9*H*-fluoren-2-yl) benzonitrile (M1). The compounds of 2,7-dibromo-9,9-dioctyl-9*H*-fluorene (7.5 mmol, 4.125 g), (4-cyanophenyl) boronic acid (5 mmol, 735 mg) and K_2CO_3 (2 M) were dissolved in toluene and stirred at room temperature, to which $Pd(PPh_3)_4$ was added under a nitrogen atmosphere. The reaction mixture was refluxed for 10 h, and then cooled to room temperature, and extracted three times with dichloromethane. The combined organic phases were washed with water and brine, successively, and then dried with $MgSO_4$. After filtration and solvent evaporation under reduced pressure, the crude product was purified by silica gel column chromatography (silica gel, hexane) to afford 1.82 g (yield: 70.1%) as a pale-yellow powder. ^1H NMR (600 MHz, $CDCl_3$) δ = 7.75 (s, 5H), 7.55–7.60 (m, 2H), 7.51 (d, J = 1.3 Hz, 1H), 7.48 (dd, J = 1.8, 6.1 Hz, 2H), 1.95–2.00 (m, 4H), 1.18 (dd, J = 6.9, 14.1 Hz, 4H), 1.01–1.13 (m, 16H), 0.78–0.82 (m, 6H), 0.63 (dt, J = 7.1, 18.1 Hz, 4H).

Synthesis of TPA-DFCP. The compounds of **M1** (3 mmol, 1.853 g), (4-(diphenylamino)phenyl)boronic acid (3 mmol, 867 mg) and K_2CO_3 (2 M) were dissolved in toluene and stirred at room temperature, to which $Pd(PPh_3)_4$ was added under nitrogen atmosphere protection. Then, the reaction mixture was refluxed for 4 h, and then cooled to room temperature, and extracted three times with dichloromethane. The combined organic phases were washed with water and brine, successively, and then dried with $MgSO_4$. After filtration and solvent evaporation under reduced pressure, the crude product was purified by silica gel column chromatography (silica gel, hexane) to afford 1.82 g (yield: 73.7%) as a white powder. ^1H NMR (600 MHz, $CDCl_3$) δ = 7.70–7.79 (m, 6H), 7.50–7.58 (m, 6H), 7.26 (t, J = 7.9 Hz, 4H), 7.14 (dd, J = 11.2, 8.2 Hz, 6H), 7.02 (t, J = 7.4 Hz, 2H), 1.96–2.06 (m, 4H), 1.10–1.19 (m, 4H), 0.99–1.10 (m, 16H), 0.76 (t, J = 7.2 Hz, 6H), 0.68 (dd, J = 6.6, 15.8 Hz, 4H). ^{13}C NMR (101 MHz, $CDCl_3$) δ 152.01, 151.77, 147.66, 147.24, 146.17, 141.66, 140.09, 139.09, 137.69, 135.34, 132.59, 129.32, 127.82, 127.71, 126.27, 125.70, 124.43, 123.95, 123.00, 121.46, 120.98, 120.32, 120.23, 119.13, 110.52, 55.38, 40.40, 31.77, 29.98, 29.20, 29.18, 23.80, 22.60, 14.07. MS (MALDI-TOF, m/z), found: $[M^+ \text{ matrix}]^+$ 735.46439; calcd for $C_{54}H_{58}N_2$: $[M^+ \text{ matrix}]^+$ 735.46728. Elemental anal. found: C, 88.24; H, 7.95; N, 3.81%; $C_{54}H_{58}N_2$: C, 88.78; H, 7.36; N, 3.86%.

Conflicts of interest

There are no conflicts to declare.

Acknowledgements

This work was financial supported by the National Natural Scientific Foundation of China (61775155, 61705156), Key R&D Program of Shanxi Province (201903D121100, 201903D421087), and Natural Science Foundation of Shanxi Province (201901D111108). We also thank professor Runfeng Chen in Nanjing University of Posts and Telecommunications for calculation data.

References

1 (*a*) P. Tao, Y. Miao, H. Wang, B. Xu and Q. Zhao, *Chem. Rec.*, 2019, **19**, 1531–1561; (*b*) P. Tao, S.-J. Liu and W.-Y. Wong, *Adv. Opt. Mater.*, 2020, 2000985.

2 Q. Wei, N. Fei, A. Islam, T. Lei, L. Hong, R. Peng, X. Fan, L. Chen, P. Gao and Z. Ge, *Adv. Opt. Mater.*, 2018, **6**, 1800512.

3 H. Usta, D. Alimli, R. Ozdemir, E. Tekin, F. Alkan, R. Kacar, A. G. Altas, S. Dabak, A. G. Gürek, E. Mutlugun, A. F. Yazici and A. Can, *J. Mater. Chem. C*, 2020, **11**, 44474–44486.

4 D. Khim, K. J. Baeg, J. Kim, M. Kang, S. H. Lee, Z. Chen, A. Facchetti, D. Y. Kim and Y. Y. Noh, *ACS Appl. Mater. Interfaces*, 2013, **5**, 10745–10752.

5 C.-L. Ho and W.-Y. Wong, *New J. Chem.*, 2013, **37**, 1665.

6 Y. Miao, K. Wang, B. Zhao, L. Gao, P. Tao, X. Liu, Y. Hao, H. Wang, B. Xu and F. Zhu, *Nanophotonics*, 2018, **7**, 295–304.

7 Y. Dong, S. Ma, X. Zhang, J. Qian, N. Zhu, B. Xu, C.-L. Ho, W. Tian and W.-Y. Wong, *Sci. China: Chem.*, 2018, **62**, 212–219.

8 Y. Liu, L. Zhang, H. Lee, H.-W. Wang, A. Santala, F. Liu, Y. Diao, A. L. Briseno and T. P. Russell, *Adv. Energy Mater.*, 2015, **5**, 1500195.

9 S.-H. Lee, B. Lim, M. Pei, H. Yang and Y.-Y. Noh, *J. Mater. Chem. C*, 2018, **6**, 7604–7611.

10 R. Capelli, S. Toffanin, G. Generali, H. Usta, A. Facchetti and M. Muccini, *Nat. Mater.*, 2010, **9**, 496–503.

11 Y. Im, S. Y. Byun, J. H. Kim, D. R. Lee, C. S. Oh, K. S. Yook and J. Y. Lee, *Adv. Funct. Mater.*, 2017, **27**, 1603007.

12 J. H. Jou, S. Kumar, A. Agrawal, T.-H. Li and S. Sahoo, *J. Mater. Chem. C*, 2015, **3**, 2974–3002.

13 K. Wang, F. Zhao, C. Wang, S. Chen, D. Chen, H. Zhang, Y. Liu, D. Ma and Y. Wang, *Adv. Funct. Mater.*, 2013, **23**, 2672–2680.

14 W.-C. Chen, C.-S. Lee and Q.-X. Tong, *J. Mater. Chem. C*, 2015, **3**, 10957.

15 J. Tagare and S. Vaidyanathan, *J. Mater. Chem. C*, 2018, **6**, 10138–10173.

16 D. Y. Kondakov, T. D. Pawlik, T. K. Hatwar and J. P. Spindler, *J. Appl. Phys.*, 2009, **106**, 124510.

17 H. Uoyama, K. Goushi, K. Shizu, H. Nomura and C. Adachi, *Nature*, 2012, **492**, 234–238.

18 D. Y. Kondakov, *Philos. Trans. R. Soc., A*, 2015, **373**, 20140321.

19 J.-H. Lee, C.-H. Chen, P.-H. Lee, H.-Y. Lin, M.-K. Leung, T.-L. Chiu and C.-F. Lin, *J. Mater. Chem. C*, 2019, **7**, 5874–5888.

20 S. Wang, M. Qiao, Z. Ye, D. Dou, M. Chen, Y. Peng, Y. Shi, X. Yang, L. Cui, J. Li, C. Li, B. Wei and W. Y. Wong, *iScience*, 2018, **9**, 532–541.

21 Z. Yang, Z. Mao, Z. Xie, Y. Zhang, S. Liu, J. Zhao, J. Xu, Z. Chi and M.-P. Aldredb, *Chem. Soc. Rev.*, 2017, **46**, 915–1016.

22 B. Chen, B. Liu, J. Zeng, H. Nie, Y. Xiong, J. Zou, H. Ning, Z. Wang, Z. Zhao and B.-Z. Tang, *Adv. Funct. Mater.*, 2018, **28**, 1803369.

23 C. Wu, B. Wang, Y. Wang, J. Hu, J. Jiang, D. Ma and Q. Wang, *J. Mater. Chem. C*, 2019, **7**, 558–566.

24 A.-D. Gorse and M. Pesquer, *J. Phys. Chem.*, 1995, **99**, 4039–4049.

25 M. Segal, M. Singh, K. Rivoire, S. Difley, T. Van Voorhis and M. A. Baldo, *Nat. Mater.*, 2007, **6**, 374–378.

26 W. Li, Y. Pan, R. Xiao, Q. Peng, S. Zhang, D. Ma, F. Li, F. Shen, Y. Wang, B. Yang and Y. Ma, *Adv. Funct. Mater.*, 2014, **24**, 1609–1614.

27 W. Li, Y. Pan, L. Yao, H. Liu, S. Zhang, C. Wang, F. Shen, P. Lu, B. Yang and Y. Ma, *Adv. Opt. Mater.*, 2014, **2**, 892–901.

28 X. Tang, Q. Bai, Q. Peng, Y. Gao, J. Li, Y. Liu, L. Yao, P. Lu, B. Yang and Y. Ma, *Chem. Mater.*, 2015, **27**, 7050–7057.

29 X. Qiu, S. Ying, C. Wang, M. Hanif, Y. Xu, Y. Li, R. Zhao, D. Hu, D. Ma and Y. Ma, *J. Mater. Chem. C*, 2019, **7**, 592–600.

30 M. Liu, X.-L. Li, D.-C. Chen, Z. Xie, X. Cai, G. Xie, K. Liu, J. Tang, S.-J. Su and Y. Cao, *Adv. Funct. Mater.*, 2015, **25**, 5190–5198.

31 Z. Q. Gao, Z. H. Li, P. F. Xia, M. S. Wong, K. W. Cheah and C. H. Chen, *Adv. Funct. Mater.*, 2007, **17**, 3194–3199.

32 C. C. Wu, Y. T. Lin, K. T. Wong, R. T. Chen and Y. Y. Chien, *Adv. Mater.*, 2004, **16**, 61–65.

33 X. Xing, L. Zhang, R. Liu, S. Li, B. Qu, Z. Chen, W. Sun, L. Xiao and Q. Gong, *ACS Appl. Mater. Interfaces*, 2012, **4**, 2877–2880.

34 L. Xiao, M. Bian, Z. Zhao, Y. Li, Q. Li, Z. Chen, D. Zhang, S. Wang, Z. Bian, Z. Liu and L. Duan, *J. Mater. Chem. C*, 2018, **6**, 745–753.

35 S. Peng, Y. Zhao, C. Fu, X. Pu, L. Zhou, Y. Huang and Z. Lu, *Chemistry*, 2018, **24**, 8056–8060.

36 H. Usta, D. Alimli, R. Ozdemir, S. Dabak, Y. Zorlu, F. Alkan, E. Tekin and A. Can, *ACS Appl. Mater. Interfaces*, 2019, **11**, 44474–44486.

37 B. Li, G. Tang, L. Zhou, D. Wu, J. Lan, L. Zhou, Z. Lu and J. You, *Adv. Funct. Mater.*, 2017, **27**, 1605245.

38 M. Hou, H. Wang, Y. Miao, H. Xu, Z. Guo, Z. Chen, X. Liao, L. Li, J. Li and K. Guo, *ACS Appl. Energy Mater.*, 2018, **1**, 3243–3254.

39 W.-C. Chen, G.-F. Wu, Y. Yuan, H.-X. Wei, F.-L. Wong, Q.-X. Tong and C.-S. Lee, *RSC Adv.*, 2015, **5**, 18067–18074.

40 B. Liu, Y. Yuan, D. He, D. Y. Huang, C. Y. Luo, Z. L. Zhu, F. Lu, Q. X. Tong and C. S. Lee, *Chemistry*, 2016, **22**, 12130–12137.